Proceedings of HT-FED2004
2004 ASME Heat Transfer/Fluids Engineering Summer Conference
July 11-15, 2004, Charlotte, North Carolina, USA

HT-FED2004-56115

INDUCER HYDRODYNAMIC FORCES IN A CAVITATING ENVIRONMENT

Stephen Skelley
NASA/Marshall Space Flight Center
MSFC, AL 35812

ABSTRACT

Marshall Space Flight Center has developed and demonstrated a measurement device for sensing and resolving the hydrodynamic loads on fluid machinery. The device - a derivative of the six-component wind tunnel balance – senses the forces and moments on the rotating device through a weakened shaft section instrumented with a series of strain gauges. This "rotating balance" was designed to directly measure the steady and unsteady hydrodynamic loads on an inducer, thereby defining the amplitude and frequency content associated with operating in various cavitation modes. The rotating balance was calibrated statically using a dead-weight load system in order to generate the 6 x 12 calibration matrix later used to convert measured voltages to engineering units. Structural modeling suggested that the rotating assembly first bending mode would be significantly reduced with the balance's inclusion. This reduction in structural stiffness was later confirmed experimentally with a hammer-impact test. This effect, coupled with the relatively large damping associated with the rotating balance waterproofing material, limited the device's bandwidth to approximately 50 Hertz. Other pre-test validations included sensing the test article rotating assembly built-in imbalance for two configurations and directly measuring the assembly mass and buoyancy while submerged under water. Both tests matched predictions and confirmed the device's sensitivity while stationary and rotating. The rotating balance was then demonstrated in a water test of a full-scale Space Shuttle Main Engine high-pressure liquid oxygen pump inducer. Experimental data was collected a scaled operating conditions at three flow coefficients across a range of cavitation numbers for the single inducer geometry and radial clearance. Two distinct cavitation modes were observed: symmetric tip vortex cavitation and alternate-blade cavitation. Although previous experimental tests on the same inducer demonstrated two additional cavitation modes at lower inlet pressures, these conditions proved unreachable with the rotating balance installed due to the intense dynamic environment. The sensed radial load was less influenced by flow coefficient than by cavitation number or cavitation mode although the flow coefficient range was relatively narrow. Transition from symmetric tip vortex to alternate-blade cavitation corresponded to changes in both radial load magnitude and radial load orientation relative to the inducer. Sensed moments indicated that the effective load center moved downstream during this change in cavitation mode. An occurrence of "higher-order cavitation" was also detected in both the stationary pressures and the rotating balance data although the frequency of the phenomena was well above the reliable bandwidth of the rotating balance. In summary the experimental tests proved both the concept and device's capability despite the limitations and confirmed that hydrodynamically-induced forces and moments develop in response to the unbalanced pressure field, which is, in turn, a product of the cavitation environment.

INTRODUCTION

The experimental tests were proposed in response to recent experiences with turbomachinery cavitation, especially in systems using liquid oxygen, and the potentially catastrophic effects of this hydrodynamic phenomenon. High-performance rocket engine systems by design operate near the limits of structural integrity and often encounter unexpected phenomena, which, in turn, may trigger unexpected system responses such as excessive vibration, rotating and stationary component contact, or elevated bearing loads. Any or all of these system responses may stem from a relatively small area of intense cavitation, and are often amplified by system structural modes or rotordynamic performance. An example of system response to pump cavitation includes the high vibration intensities detected during development of the Space Shuttle Main Engine Alternate Turbopump and described by Ryan (1994). More recently, water flow tests by Zoladz (2000) and component-level testing of more aggressive inducer designs resulted in varying levels of inducer blade damage. Figure 1 shows the more dramatic consequence of excessive hydrodynamic loads

with complete failure of each inducer blade tip. A 1999 investigation into the Japanese H-II-8F launch vehicle failure (2000) identified intense cavitation at the turbopump inlet as the most likely cause of inducer blade breakage and subsequent vehicle destruction.

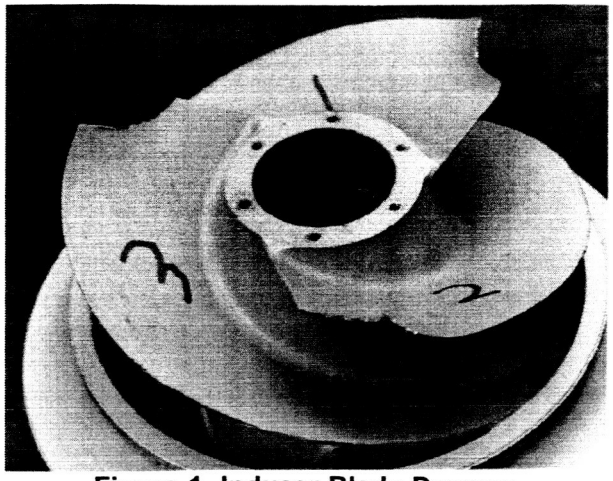

Figure 1. Inducer Blade Damage

Despite these dramatic examples, no description of both the amplitude and frequency content of any cavitation-induced, hydrodynamic loads has been published for any inducer design despite Rosenmann's (1965) original investigation into this phenomenon. As Rosenmann, Acosta (1958), and Iura (1958) have confirmed, even and odd number blade inducers often exhibit both stable and rotating cavitation modes depending on the pump operating conditions, whereby cavitation "cells" may attach themselves to the inducer blades or propagate around the inducer periphery. The pressure imbalance caused by the attached or rotating cavitation cells necessarily develops a force imbalance, which exerts itself on the rotating assembly as a stationary or rotating radial load. The axial location of this radial load moves as the cavitation intensity increases and the inducer flow passages fill with vapor. The cavitation cell number and rotation rate determine the radial load excitation frequency. Whether this excitation force interacts with system structural modes or not depends on the pump operating condition, the system response characteristics, and the relative damping.

ROTATING BALANCE

The following section summarizes the mechanical design, instrumentation, and static calibration of the rotating balance.

ROTATING BALANCE MECHANICAL DESIGN

The rotating balance was essentially based on the static wind tunnel balance concept and the approach used to design the flexures was a combination of established methods and more recent experiences with similar design produced for the United States Navy and United Technologies Research Center. The intent was to produce a compact device capable of sensing the hydrodynamically-induced forces generated by an inducer operating in cavitated conditions and resolving the axial and circumferential locations of these forces relative to the inducer. Measurement of six components - normal force, side force, and axial force and pitch moment, yaw moment, and roll moment - were required to locate the integrated load position. The load range requirements summarized in Table 1 then dictated the flexure design and strain gauge requirements. Balance orientation is shown in Figure 2.

NOMENCLATURE

N	=	Shaft Speed {rev/min}	NF	=	Normal Force {pounds-force}
Q	=	Volumetric Flow Rate {gallon/min}	SF	=	Side Force {pounds-force}
P_{T1}	=	Inlet Total Pressure {pounds-force/inch^2}	AF	=	Axial Force {pounds-force}
P_{T2}	=	Exit Total Pressure {pounds-force/inch^2}	PM	=	Pitch Moment {inch-pounds-force}
P_v	=	Water Vapor Pressure {pounds-force/inch^2}	YM	=	Yaw Moment {inch-pounds-force}
ρ	=	Water Density {pounds-mass/foot^3}	RM	=	Roll Moment {inch-pounds-force}

D_T	=	Inducer Tip Diameter	=	*5.160 inch*
D_H	=	Inducer Hub Diameter	=	*3.050 inch*
L	=	Inducer Axial Length {inch}	=	*1.946 inch*
g_c	=	Constant	=	*32.174 pounds-mass-foot/pounds-force-second^2*
U	=	Inducer Leading Edge Tip Speed {ft/sec}	=	$\pi D_T N / 720$
Nss	=	Suction Specific Speed {rpm-gpm$^{1/2}$/ft$^{3/4}$}	=	$N Q^{0.5}/[(P_{T1}-P_v)\ 144 / \rho]^{0.75}$
ψ	=	Head Coefficient	=	$144\ (P_{T2}-P_{T1})\ g_c / (\rho U^2)$
ϕ	=	Inlet Tip Flow Coefficient	=	$1.283\ Q / [\pi\ (D_T^2 - D_H^2)\ U]$

Forces Normalized by $0.5\ \rho\ U^2\ \pi\ D_T L$ Moments Normalized by $0.5\ \rho\ U^2\ \pi\ D_T L^2$

ROTATING BALANCE INSTRUMENTATION AND CALIBRATION

The balance flexures were instrumented with semiconductor-type, uni-directional strain gauges arranged in 6 bridges – one for each of the 6 measured components - consisting of from 8 to 16 individual gauges. The instrumented device was waterproofed by the application of a continuous layer of room temperature vulcanizer. Bridge integrity was verified before and after a water immersion test and after confirmation, the balance was calibrated statically across its intended load range. A calibration fixture and moment arm assembly was used to apply the full range of load combinations, from which the primary and secondary, or interaction, coefficients were calculated. The resulting 6 x 12 calibration matrix in Table 2 was used to convert sensed voltages to engineering units. Estimated measurement error for each component as a percent of full scale also appears in Table 2. The intended goal of 1% full scale or less for each sensed component accuracy was satisfied.

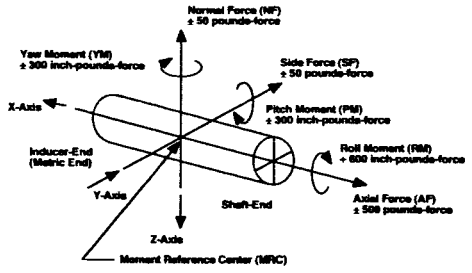

Figure 2. Rotating Balance Component Orientation

Table 1. Rotating Balance Components

Component	Load Range
Normal Force (NF)	± 50 pounds-force
Side Force (SF)	± 50 pounds-force
Axial Force (AF)	± 500 pounds-force
Pitch Moment (PM)	± 300 inch-pounds-force
Yaw Moment (YM)	± 300 inch-pounds-force
Roll Moment (RM)	± 600 inch-pounds-force

Table 2. Balance Static Calibration Matrix

Interaction Coefficients	Component					
	NF	PM	SF	YM	RM	AF
NF	1.9711E-02	5.6247E-01	-2.9632E-03	-3.6003E-04	6.7089E-03	0.0000E+00
PM	1.2699E-02	5.9365E-02	4.8497E-04	-6.5597E-04	1.6306E-03	4.7540E-03
SF	-3.7769E-03	-2.4474E-03	1.9841E-02	5.6038E-01	-1.5641E-03	0.0000E+00
YM	6.2081E-05	-1.4034E-03	1.1965E-02	6.0062E-02	1.9024E-04	-2.5455E-03
RM	3.1189E-03	-5.8331E-04	-1.2677E-03	1.8419E-03	4.4763E-02	0.0000E+00
AF	8.0683E-04	7.7521E-03	-1.4655E-04	-3.2904E-03	1.1425E-04	8.5287E-02
NF^2	5.6541E-05	3.2500E-05	2.5043E-06	0.0000E+00	-4.1259E-05	0.0000E+00
PM^2	1.0696E-06	-1.2785E-05	0.0000E+00	4.8779E-07	7.1438E-07	7.7018E-06
SF^2	-4.2869E-06	0.0000E+00	-9.7384E-06	-6.0634E-05	0.0000E+00	0.0000E+00
YM^2	-5.9069E-07	-1.5518E-06	6.0694E-07	-1.6958E-05	0.0000E+00	6.6065E-06
RM^2	7.2274E-07	9.3816E-08	1.3467E-08	-1.2136E-07	-2.2892E-06	-3.5818E-07
AF^2	-2.1571E-07	4.1968E-07	-4.7999E-07	7.6642E-06	0.0000E+00	3.7048E-06
Percent Full Scale Error (2σ level)	0.58%	0.46%	0.61%	0.34%	0.26%	0.48%

EXPERIMENTAL TEST ARTICLE

The rotating balance was installed in an existing test article with minor modifications to the existing hardware. As shown in Figure 3, the test article included a full-scale replica of the Space Shuttle Main Engine (SSME) high-pressure liquid oxygen inducer in an axial inlet configuration. The SSME inducer shown in Figure 4 was selected due to its known cavitation performance, described by Bordelon (1995). The six-vane inlet guide assembly provided the required inlet velocity profile. Discharge flow was collected and guided away from the test article in a generic volute with radial exit. The inducer itself included 4 main blades with moderately swept leading edges. The minor modifications to the existing hardware included separating the inducer inlet fairing from the rotating assembly to reduce the overhung mass. Likewise, the exit diffuser cone was modified to increase the radial clearance around the rotating balance. A small amount of fluid was bled from the main flow and circulated through the rotating balance cavity to stabilize the balance temperature and mitigate any temperature effects on the strain gauges. This leakage flow was extracted downstream of the inducer discharge and returned to the primary flow through the axial clearance just upstream of the inducer leading edge. Two holes in the inducer nut metered this flow and leakage rates of no more than 0.05% of primary flow rate were estimated. A radial clearance of 0.030 ± 0.002 inch (0.762 ± 0.051 mm) was maintained around the inducer to minimize asymmetry-induced radial loads. A photograph of the rotating balance appears in Figure 5. A photograph of the test article installed in the facility appears in Figure 6.

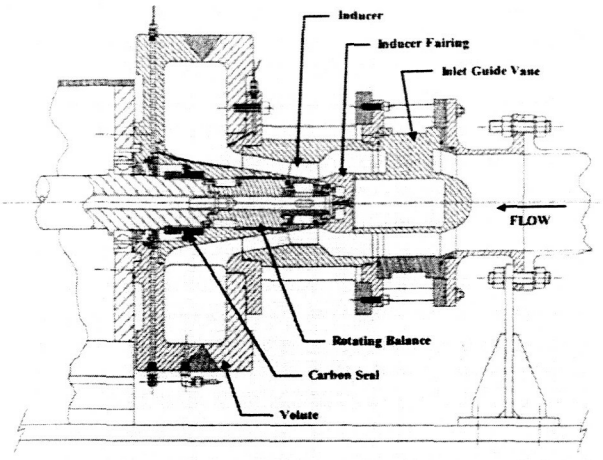

Figure 3. Test Article Cross Section

Figure 4. SSME Inducer

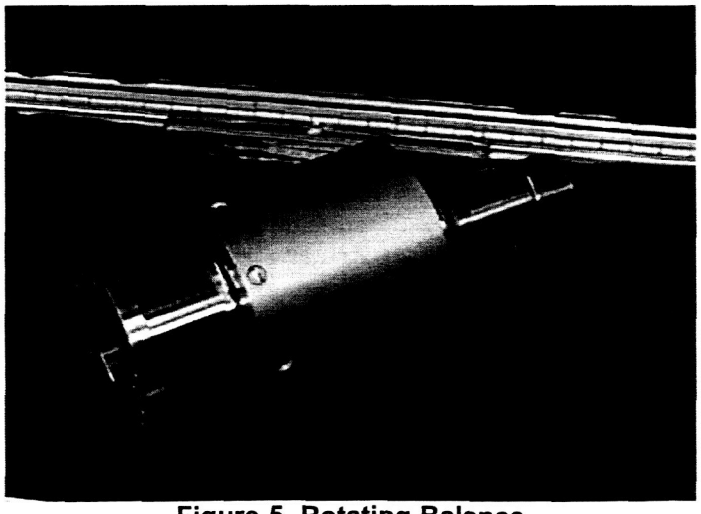

Figure 5. Rotating Balance

Figure 6. Experimental Test Article

MEASUREMENTS AND DATA ACQUISITION

A combination of steady state and high-frequency response devices were used to measure both inducer and balance performance and to monitor balance health. Steady state pressures were located along the flow path outer diameter both upstream, along the inducer shroud, and downstream of the inducer. Total pressure upstream of the inlet guide vane assembly was measured with a single, shrouded Kiel probe. Likewise, 3 total pressure rakes, with 3 shrouded, total pressure taps each, were installed downstream of the inducer discharge and aligned with the inducer exit flow angle. Flow rate was sensed via a 6-inch turbine-type flow meter while shaft speed was sensed through a magnetic collar and pickup device. High-frequency-response pressure transducers were located upstream of the inducer, at the leading edge, the inducer mid-chord, and slightly downstream of the inducer for complete mapping of the unsteady environment. At the inducer leading edge and downstream location, 3 transducers were included for cavitation cell train phase identification. Bearing outer race, slip ring, and water temperatures were also recorded.

Two semi-parallel systems were employed for data acquisition; one consisting of a LabView-based analog-to-digital converter with relatively limited bandwidth, the second a true high-frequency, 32-channel data system with a measurement bandwidth of 10,000 Hertz. A common power supply provided the required 5 volts to the balance bridges. The LabView-based system continuously sampled balance voltages, held these values in a buffer, and displayed or stored averaged values of voltage and processed engineering units. This system provided "averaged" or DC values and also served as a health monitor. The high-frequency data acquisition system recorded both balance voltages as well as test article operating conditions, unsteady shroud pressures, and accelerations. A second LabView-based system was used to collect and process the steady state measurements such as pressures, temperatures, flow rate, speed, and differential pressures. Steady state data was sampled from 100 to 1000 times and the population mean and standard deviation stored in engineering units.

EXPERIMENTAL TEST PLAN

The experimental test included three series: 1) modal test, 2) air spin test, and 3) water test. The incremental approach allowed the rotating balance performance to be monitored under increasingly harsh operating conditions, thereby building confidence while minimizing risk to the device. The modal test was conducted to measure the assembly's structural response at various excitation frequencies. This data would later be used to define the upper limit of the rotating balance's measurement bandwidth. Likewise, the air spin test was conducted to directly measure the rotating assembly's imbalance up to a maximum operating speed of 5000 revolutions per minute. This data would be subtracted from the measured data in water to remove the built-in static load. The final test series included operating at scaled conditions in water from 80% to 120% of the design flow coefficient. The original test plan included water testing from non-cavitated condition to complete head breakdown. Unfortunately, rotating balance load limits prevented testing at the highest suction specific speeds. Table 3 summarizes the test series details and operating conditions.

Table 3. Experimental Test Series

Series	Percent Reference Flow Coefficient	Suction Specific Speed	Speed (rpm)	Comments
Modal Test	N/A	N/A	0	Carbon Seal Removed
Air Spin	N/A	N/A	300 - 5000	Carbon Seal Removed
Water Test 1	90% - 110%	5000 - Balance Load Limit	2200, 3200, 3800	High Frequency Data Only
Water Test 2	80% - 120%	5000 - Balance Load Limit	2200, 3200, 3800	Steady Performance Data Only

Reference Flow Coefficient = 0.161

ROTATING BALANCE DATA REDUCTION

Electrical zeros were extracted from the periodic output generated by slowly rotating the assembly through two complete revolutions. This procedure was repeated at regular intervals to compensate for any drift or thermal effects. Sensed voltages were then converted to engineering units by first subtracting the measured electrical zeros from each component and then processing the resulting voltages through the calibration matrix. The method from Smith (1972) was used, whereby the calibration matrix was converted to three matrices representing the primary sensitivities and the first and second order interaction coefficients. Data across the entire measured bandwidth was processed in this fashion by the high-frequency data system.

RESULTS

Experimental results from the four experimental test series are summarized.

MODAL TEST RESULTS

A modal test was conducted in June of 2001 following test article installation into the test facility. The test was conducted in-situ to insure that all relevant structural contributions would be accurately captured since the modal test output – structural amplification versus excitation frequency – would be used to limit or correct all rotating balance measurements. Figure 7 shows the experimental results with structural amplification factor versus frequency for each sensed load component. The first measured structural mode at 225 Hertz compared favorably to the predicted value of 217 Hertz. The relatively large damping, however, was surprising and ultimately led to limiting all rotating balance data to approximately 34 Hertz and below. This selected upper limit corresponds to a structural magnification of 5%. As such, rotating balance results presented here, except where noted, have been restricted to 34 Hertz and below.

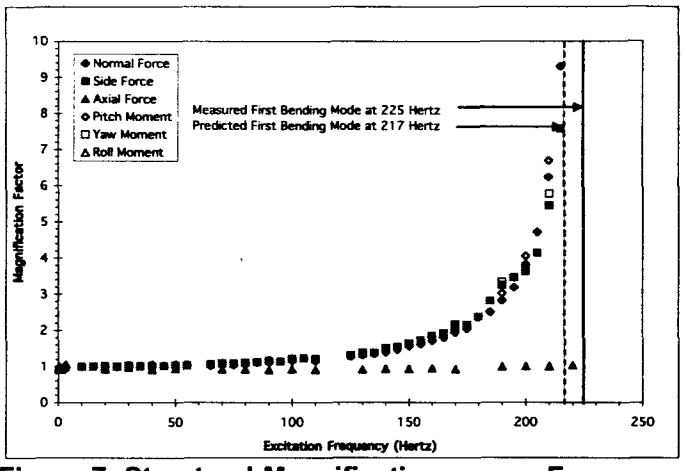

Figure 7. Structural Magnification versus Frequency

AIR SPIN RESULTS

Two air spin tests were conducted to verify the balance sensitivity and directly measure the built-in imbalance. Results appear in Figure 8. The first test included a small weight attached to the rotating assembly, off the axis of rotation to induce a small radial load. The measured imbalance was 0.542 ± 0.018 ounce-inch (390 ± 13.0 gram-millimeter) at an angle of –74.7 ± 1.4 degrees relative to NF. The second test did not include the added weight and replicated the water test configuration. A total imbalance of 0.058 ± 0.015 ounce-inch (41.8 ± 10.8 gram-millimeter) at an angle of 81.9 ± 1.4 degrees relative to NF was measured for the clean assembly. The difference between tests, 0.596 ± 0.023 ounce-inch (429 ± 16.6 gram-millimeter), matched the predicted difference of 0.596 ± 0.022 ounce-inch (429 ± 15.8 gram-millimeter) based on the added weight geometry and location. The clean assembly imbalance has been subtracted from all values presented here. This value was also well below the maximum estimated imbalance of 0.107 ounce-inch (77.0 gram-millimeter) based on the individual component allowable imbalances and assembly tolerances

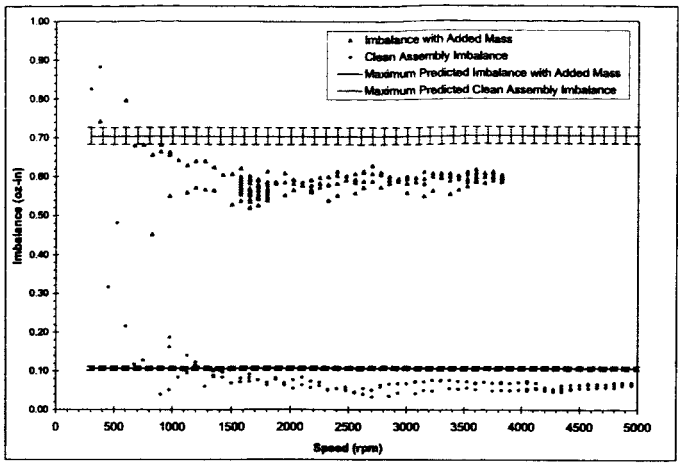

Figure 8. Measured Imbalance in Air versus Speed

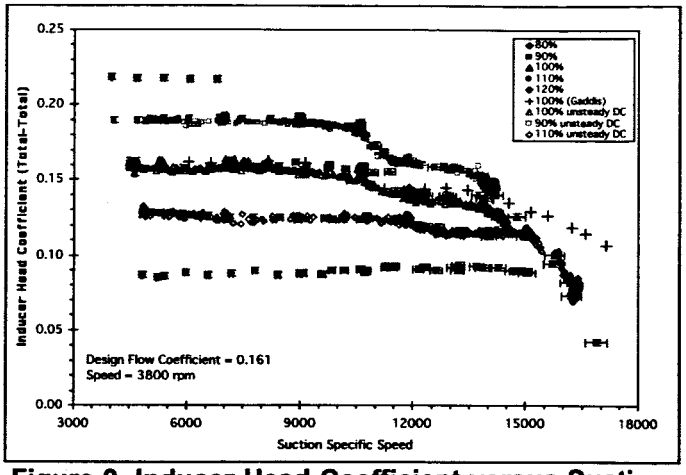

Figure 9. Inducer Head Coefficient versus Suction Specific Speed and Flow Coefficient at 3800 rpm

WATER FLOW TEST RESULTS

Sufficient measurements were incorporated into the test article to verify inducer steady state performance both to insure that hydrodynamic performance matched that from previous experimental tests of the same inducer and to compute inducer performance parameters. The inducer suction performance appears in Figure 9 versus percent reference flow coefficient along with experimental data at the same flow coefficient from a previous water flow test by Gaddis (1997). For comparison the corresponding data from the high-frequency response data system ("Unsteady DC") is included. The reductions in steady head rise at 90% and 100% of the design flow coefficient were previously observed to correspond with the transition from a steady, four-blade cavitation mode to an alternate blade cavitation mode. The measured composite, 2 x synchronous (2 x N), and 4 x synchronous (4 x N)-averaged unsteady pressures at the inducer inlet at the reference flow coefficient at 3800 revolutions per minute are plotted in Figure 10 versus suction specific speed. The high-frequency response devices provide a more accurate indication of cavitation mode and illustrate the contribution of these harmonics to the total fluctuating pressure intensity. That the 2 x N and 4 x N oscillations coexist between suction specific speeds of 10,000 to 14,000 indicates that the transition is indistinct, and that asymmetric pressure distributions may result.

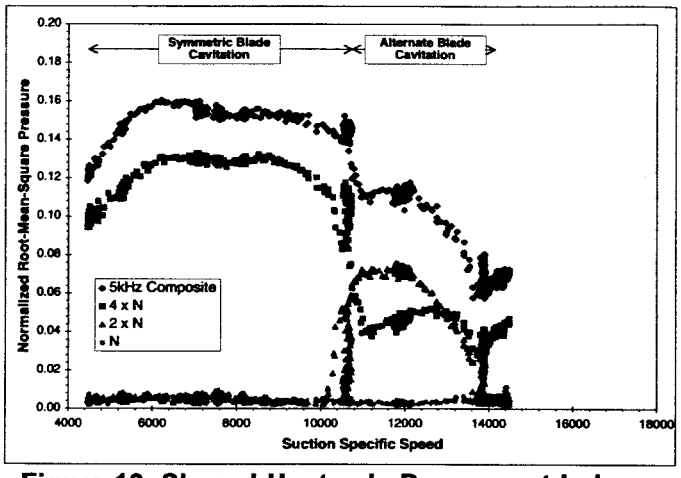

Figure 10. Shroud Unsteady Pressure at Inducer Inlet versus Suction Specific Speed at Reference Flow Coefficient and 3800 rpm

Since the rotating balance measurements were severely hampered by potential structural magnification at higher frequencies, essentially only the DC values for the sensed forces and moments were considered valid. Although this restriction eliminated all the higher-frequency-content data, the sensed loads confirmed that the device could accurately detect the magnitude and relative orientation of the integrated hydrodynamic forces. The radial load magnitudes in Figure 11, developed in response to the evolving pressure field, increased with increasing cavitation intensity (increasing suction specific speed) until the cavitation environment itself adjusted to a more stable regime – alternate blade cavitation. The load magnitude then seemed to "reset" to a lower value at a suction specific speed of approximately 11,000 and again slowly increased from the new minimum. At a suction specific speed of approximately 14,000, the radial load again shifted in response to the adjusting pressure field. At this upper suction specific speed, however, the transition in cavitation mode was less precise and possibly incomplete, as exhibited by the coexistence of the 2 x N and 4 x N oscillations in Figure 10.

The highly incoherent unsteady environment suggested that this operating condition was on the edge of switching to Bordelon's "long, symmetric cavities." The relative angle of the resultant load also changed, essentially rotating around the periphery by approximately 90 degrees in response to the unstable and developing pressure field. Results from Karyeaclis (1989), Bhattacharyya (1997), and Rosenmann are included for comparison only as each were from different inducers, flow coefficients, etc. The off-design cases in Figures 12 and 13 exhibited similar trends with relatively constant radial load magnitude and angle during the symmetric cavitation and changes in both angle and magnitude with the onset of alternate blade cavitation. The highest flow coefficient (110% of the reference) produced the largest change in radial load in the transition from symmetric to alternate blade cavitation.

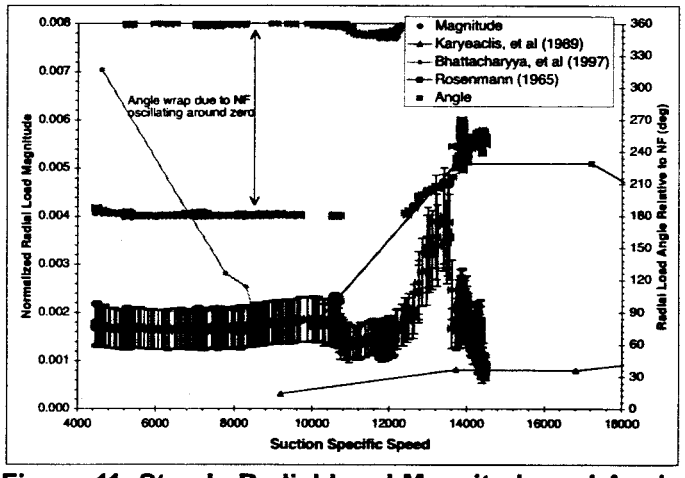

Figure 11. Steady Radial Load Magnitude and Angle versus Suction Specific Speed at Reference Flow Coefficient and 3800 rpm

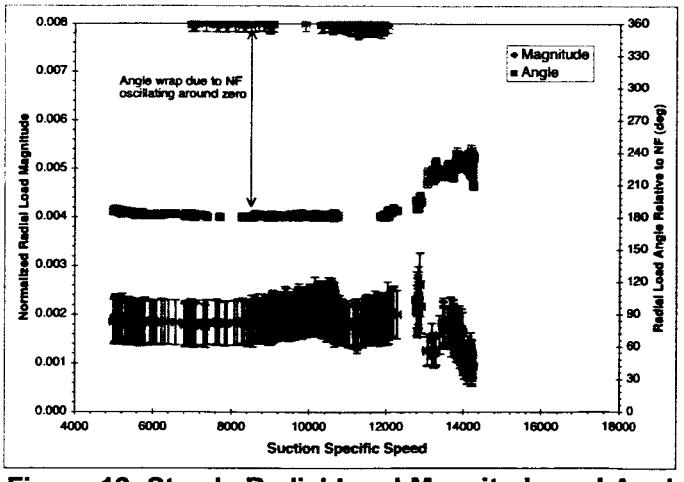

Figure 12. Steady Radial Load Magnitude and Angle versus Suction Specific Speed at 90% Reference Flow Coefficient and 3800 rpm

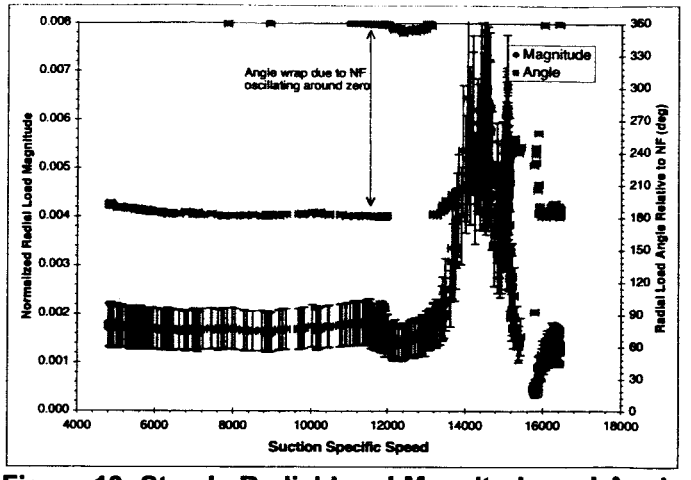

Figure 13. Steady Radial Load Magnitude and Angle versus Suction Specific Speed at 110% Reference Flow Coefficient and 3800 rpm

Pitch and yaw moments in Figure 14, 15, and 16 appeared to confirm Rosenmann's observation that the pressure environment due to increased cavitation would generate an "end couple" in addition to a net radial load. In each flow case the pitch and yaw moments declined slightly during symmetric cavitation indicating that the pressure field was "unloading" at the inducer leading edge and the resultant radial force was moving downstream with increasing suction specific speed. Like the radial load, pitch and yaw moments responded to the onset of alternate blade cavitation and the adjusted pressure field by returning to or approaching their initial values at lower suction specific speeds. The incoherence observed in the radial load angle at 110% flow near the end of the alternate blade cavitation zone was evident in the moments as well, indicating that the axial location of the net radial load was also fluctuating with the unstable pressure environment.

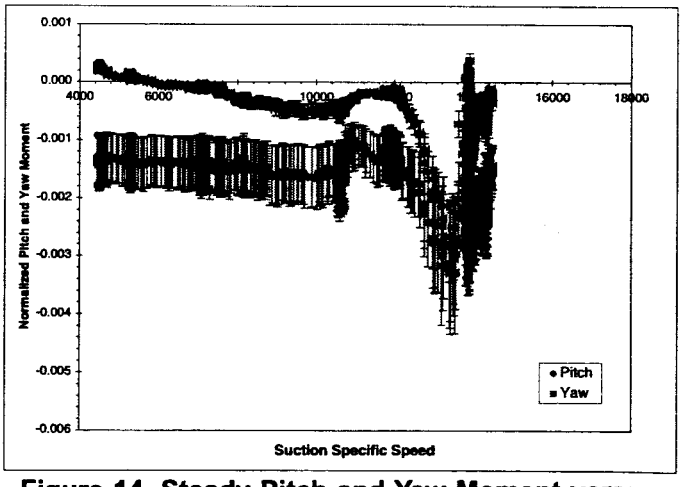

Figure 14. Steady Pitch and Yaw Moment versus Suction Specific Speed at Reference Flow Coefficient and 3800 rpm

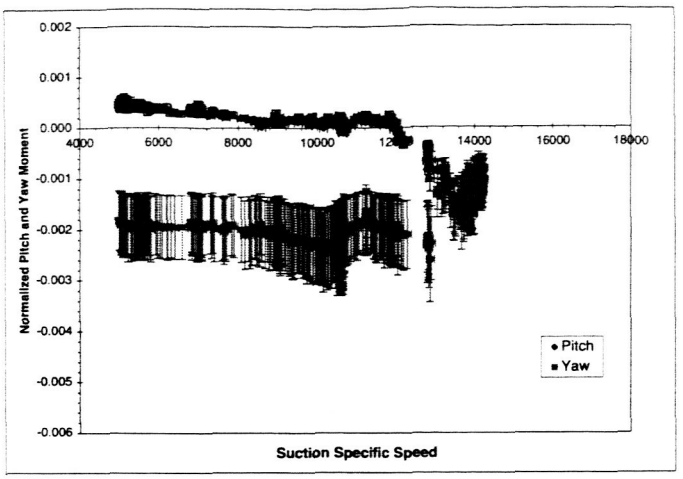

Figure 15. Steady Pitch and Yaw Moment versus Suction Specific Speed at 90% Reference Flow Coefficient and 3800 rpm

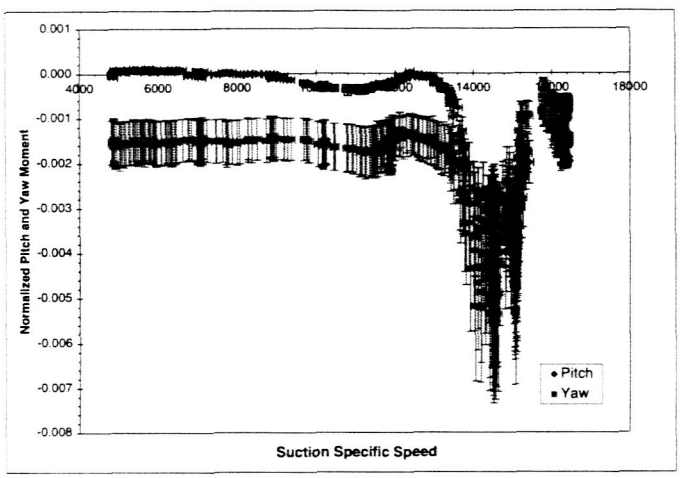

Figure 16. Steady Pitch and Yaw Moment versus Suction Specific Speed at 110% Reference Flow Coefficient and 3800 rpm

Figures 17 and 18 include spectrograms of the sensed fluctuating pressure and normal force magnitudes up to 1000 Hertz at the reference flow coefficient at 3800 revolutions per minute. Of interest here is the observed "higher-order cavitation" phenomena detected at very low suction specific speeds. Simultaneous, single-cell rotating disturbances were detected moving at 8.7 and 10.2 times shaft rotation rate in opposite directions. No previous investigations noted this phenomena. Although the rotating balance data was considered invalid above approximately 34 Hertz, Figure 18 provides a qualitative insight into the frequency content of the hydrodynamic loads corresponding to all the observed cavitation modes.

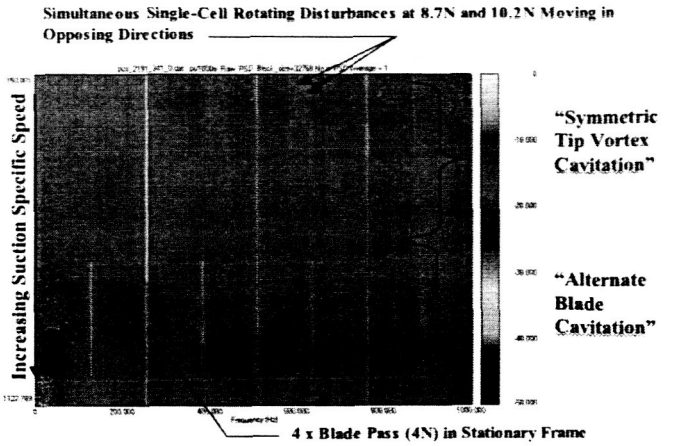

Figure 17. Unsteady Pressure Spectrogram at Inducer Leading Edge at Reference Flow Coefficient and 3800 rpm

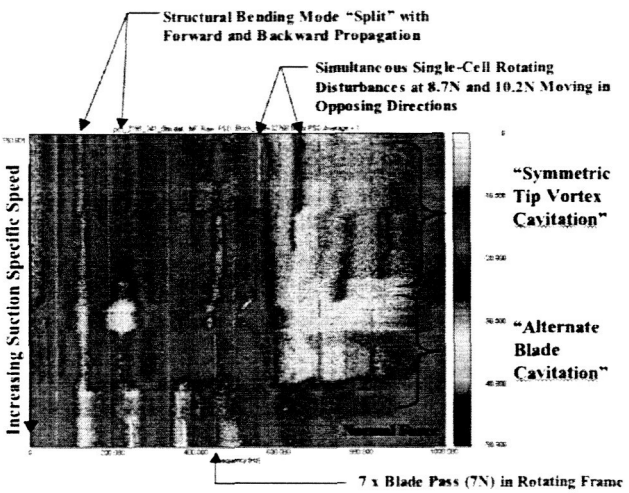

Figure 18. Normal Force Spectrogram at Reference Flow Coefficient and 3800 rpm

UNCERTAINTY ANALYSIS

An uncertainty analysis incorporating the experimental precision and bias errors using the root-sum-square method of Coleman (1989) was performed to estimate the uncertainties associated with the measured and calculated quantities. A 95% confidence level was assumed. The estimated uncertainties for each of the parameters presented here are summarized in Table 4. The relatively large uncertainties associated with the normalized radial load and moments were due to the subtraction of the imbalance from these components and the equivalent orders of magnitude of the values.

Table 4. Calculated Uncertainties

Parameter	Uncertainty
Inducer Head Coefficient (Total-Total)	0.007
Suction Specific Speed	380 rpm-gpm$^{1/2}$/ft$^{3/4}$
Normalized Radial Load Magnitude	24.9% of value
Radial Load Angle	2.0 degrees
Normalized Pitch Moment	23.6% of value
Normalized Yaw Moment	31.9% of value

SUMMARY AND CONCLUSIONS

A device for sensing and resolving the fluid-induced forces and moments on a cavitating inducer was developed and validated via water test of a well-documented inducer. The hydrodynamic force and moment results presented here, although unique, are the product of a consistent and verifiable device development. Likewise, the modal and air test results as well as the repeatable inducer performance in water were intended to insure confidence. Several observations can be made:

1) Unexpectedly high damping severely limited the rotating balance's measurement bandwidth to less than 34 Hertz.
2) The magnitude and angle of the radial force remained essentially constant during the symmetric tip vortex cavitation mode as the inherent symmetry of the pressure distribution manifested itself as a steady radial load.
3) The magnitude and angle of the radial force increased during the transition from symmetric tip vortex to alternate-blade cavitation mode. The change in sensed radial force and its direction relative to the inducer during this transition suggests that the interaction and coexistence of the unsteady phenomena impose an unbalanced pressure distribution.
4) Axial location of the integrated radial load – as sensed by changes in the pitch and yaw moments – moved downstream with increasing suction specific speed. This change in location confirms that the inducer leading edges "unload" as the vapor volume increases.
5) The magnitude and angle of the radial force is more influenced by suction specific speed or cavitation mode than by flow coefficient.
6) The expected cavitation regimes for the SSME inducer should be updated to include "higher-order" rotating cavitation.

ACKNOWLEDGMENTS

The author would like to thank the test team members who made this possible: Tom Zoladz, Richard Norman, Joey Kirkpatrick, Jeff Lindner, and Eric Earhart of Marshall Space Flight Center, and Doug McBride and Bo Jones of LB&B Associates. Micro Craft (now Alliant Techsystems) of Tullahoma, Tennessee and Modern Machine & Tool of Newport News, Virginia designed, manufactured, instrumented, and calibrated the rotating balance. Thanks also go to Wayne Bordelon of Marshall Space Flight Center for originally proposing this work and providing valuable guidance along the way. This work was funded by Marshall Space Flight Center through an internal research and development office.

REFERENCES

Acosta, A.J., 1958, "An Experimental Study of Cavitating Inducers," *Proceedings of the 2nd Symposium on Naval Hydrodynamics*, 533-557.

Bhattacharyya, A., Acosta, A.J., Brennen, C.E., and Caughey, T.K., 1997, "Rotordynamic Forces in Cavitating Inducers," *Journal of Fluids Engineering*, 119.

Bordelon, W.J., Gaddis, S.W, and Nesman, T.E., 1995, "Cavitation Environment of the Alternate High Pressure Oxygen Turbopump Inducer," ASME Fluids Engineering Division, 210.

Coleman, H.W. and Steele, W.G., 1989, Experimentation and Uncertainty Analysis for Engineers, John Wiley and Sons.

Gaddis, S.W., 1997, "Alternate Turbopump Development High Pressure Oxidizer Turbopump Second Source Inducer Water Flow Rig Test Plan," MSFC memo ED34-97-024.

Iura, T., 1958, "An Experimental Study of Cavitating Inducers," *Proceedings of the 2nd Symposium on Naval Hydrodynamics*, 554-557.

Karyeaclis, M.P., Miskovish, R.S., and Brennen, C.E., 1989, *Rotordynamic Tests in Cavitation of the SEP Inducer*, California Institute of Technology.

NASDA Report No. 96, *Launch Failure of H-II-8F Launch Vehicle: Cause of Failure Investigated through Various Analyses*, 2000.

Rosenmann, W., 1965, "Experimental Investigations of Hydrodynamically Induced Shaft Forces with a Three Bladed Inducer," *Proceedings of the ASME Symposium on Cavitation in Turbomachinery*, 172-195.

Ryan, R.S., Gross, L.A., Mills, D., and Mitchell, P., 1994, "The Space Shuttle Main Engine Liquid Oxygen Pump High-Synchronous Vibration Issue, The Problem, The Resolution Approach, The Solution," AIAA 94-3153.

Smith, D.L., 1972, *An Efficient Algorithm Using Matrix Methods to Solve Wind-Tunnel Force-Balance Equations*. NASA TN D-6860.

Zoladz, T., 2000, "Observations on Rotating Cavitation and Cavitation Surge from the Development of the Fastrac Engine Turbopump," AIAA-2000-3403.